

Secondary instability of the spike-bubble structures induced by nonlinear Rayleigh-Taylor instability with a diffuse interface

Lin Han  and Jianjie Yuan *Department of Mechanics, Tianjin University, Tianjin 300072, China*Ming Dong **State Key Laboratory of Nonlinear Mechanics, Institute of Mechanics, Chinese Academy of Sciences, Beijing 100190, China*

Zhengfeng Fan

*Institute of Applied Physics and Computational Mathematics, Beijing 100088, China
and Center for Applied Physics and Technology, Peking University, Beijing 100871, China*

(Received 3 December 2020; revised 1 September 2021; accepted 6 September 2021; published 22 September 2021)

Laminar-turbulent transition in Rayleigh-Taylor (RT) flows usually starts with infinitesimal perturbations, which evolve into the spike-bubble structures in the nonlinear saturation phase. It is well accepted that the emergence and rapid amplification of the small-scale perturbations are attributed to the Kelvin-Helmholtz-type secondary instability due to the high velocity shears induced by the stretch of the spike-bubble structures, however, there has been no quantitative description on such a secondary instability in literature. Moreover, the instability mechanism may not be that simple, because the acceleration or the “rising bubble” effect could also play a role. Therefore, based on the two-dimensional diffuse-interface RT nonlinear flows, the present paper employs the Arnoldi iteration and generalized Rayleigh quotient iteration methods to provide a quantitative study on the secondary instability. Both sinuous and varicose instability modes with high growth rates are observed, all of which are confirmed to be attributed to both the Rayleigh-Taylor and Kelvin-Helmholtz regimes. The former regime dominates the early-time instability due to the “rising bubble” effect, whereas the latter regime becomes more significant as time advances. Being similar to the primary RT instability [Yu *et al.*, *Phys. Rev. E* **97**, 013102 (2018), Dong *et al.*, *Phys. Rev. E* **99**, 013109 (2019), Fan and Dong, *Phys. Rev. E* **101**, 063103 (2020)], the diffuse interface also leads to a multiplicity of the secondary instability modes and higher-order modes are found to exhibit more local extremes than the lower-order ones. Direct numerical simulations are carried out, which confirm the linear growth of the secondary instability modes with infinitesimal amplitudes and show their evolution to the turbulent-mixing state.

DOI: [10.1103/PhysRevE.104.035108](https://doi.org/10.1103/PhysRevE.104.035108)

I. INTRODUCTION

Rayleigh-Taylor (RT) instability appears at the interface of two fluids with density disparity when the acceleration is toward the heavier fluid, which is of practical relevance to a variety of engineering applications [1–3]. Usually, the RT turbulent mixing is a consequence of the accumulation of the RT instability modes from small initial amplitudes. At the beginning they grow exponentially, until reaching the nonlinear saturation phase, in which the spike-bubble structures appear. The structures stretch longitudinally, leading to large-scale shears of the velocity field. As the subsequent small-scale perturbations appear and grow drastically, the large structures oscillate laterally, and the turbulent phase is reached eventually. Although the RT instability has been studied extensively by theoretical, numerical and experimental approaches for decades [3–11], it is still a challenging issue to construct an effective model for the prediction of the RT transition subject to given initial perturbations, such

that the time to switch on turbulence models in engineering simulations is well prescribed. This requires a comprehensive understanding of the intrinsic mechanism of the transition process.

The classical RT instability theory [12,13] was based on two fluids with a sharp interface, however, as revealed by Yu *et al.* [14], the RT flow with a diffuse interface would support a multiplicity of eigenmodes, and the most unstable one is intrinsically an extension of the single eigenmode of the sharp-interface configuration. A physical interpretation of the occurrence of the multiple-mode phenomenon was provided by Dong *et al.* [15] using the Wentzel-Kramers-Brillouin (WKB) approximation. Fan and Dong [16] further developed a theoretical model to describe the excitation of each eigenmode subject to an artificially introduced initial perturbation, and their nonlinear interaction in later phases was also characterized. The late-phase spike-bubble structures may be quite different for different initial perturbations, and the transition to turbulence could be delayed if the initial perturbations are carefully designed.

In the early nonlinear phase, the lengths of the spikes and bubbles grow linearly with time (quasiconstant spike

*dongming@imech.ac.cn

and bubble speeds), which was recognized as an asymptotic growth in the nonlinear saturation phase [1,6,17,18], while in the later nonlinear phase, the growth of the spike and bubble lengths with time becomes quadratic; see Refs. [16,19–24]. Recent direct numerical simulations [25,26] on two- and three-dimensional single-mode (single wavelength in the tangential-to-interface direction) RT instability confirm the above phenomena, although in late times the spike and bubble growths are oscillatory around the mean quadratic-growing curve. The latter was referred to as the chaotic development. However, the spike-bubble structures do not lead to transition to turbulence themselves, because their length scales are large, and there may be two regimes relating to the excitation of small-scale perturbations. The first one is the nonlinear interaction, namely the interaction of perturbations with wave numbers k_1 and k_2 would generate perturbations with wave numbers $k_1 \pm k_2$ directly, and the newly generated perturbations can also act as one of the interaction seeds, leading to a broadband response. This is essentially a cascade regime and the generated perturbations are always weaker than their seeds. Another possibility is the so-called secondary instability, in which the exponential growth of the small-scale perturbations is supported. Apparently, the latter regime is more efficient.

The Kelvin-Helmholtz (KH) instability is one of the classical problems in fluid dynamics, which is caused by the unstable interface between the fluids under the action of parallel shear flow. The KH instability is believed to be the reason for the evolution of mushroom-type structure in the nonlinear process of RT and Richtmyer-Meshkov instability, which plays a key role in the transition process [3]. Because the stretch of the spikes and bubbles leads to high shears of the moving fluids, the secondary instability is affirmed to be attributed to KH mechanism. However, the KH instability is not the only possible regime to support the secondary instability, and the acceleration may also induce small-scale instabilities since the wavy interface could generate small-scale baroclinic torque. Such a mechanism is also the case for the rising-bubble instability as studied by many previous papers [27–29]. The main task of the present paper is to present a quantitative means to confirm which regime is dominant for a certain period of time. Also, we are going to reveal the effect of the diffuse interface on the secondary instability. Finally, we will carry out direct numerical simulations (DNSs) to confirm the linear growth of the secondary instability and show their evolution to turbulent mixing.

II. MATHEMATICAL DESCRIPTIONS

A. Description of the physical problem

The physical model to be studied follows those in Refs. [14–16], a two-dimensional (2D) compressible Rayleigh-Taylor flow with a smeared interface. The densities of the heavy and light fluids are denoted as ρ_h and ρ_l , respectively, and the Atwood number $A = (\rho_h - \rho_l) / (\rho_h + \rho_l)$ is introduced to measure the density disparity. The 2D Cartesian coordinate system (x, y) is employed, with its origin o locating at the interface and x and y perpendicular and parallel to the interface, respectively. We choose

the scale connected with the maximum of the density gradient as the characteristic length scale, $L_m = \min[\rho_0^* / (d\rho_0^*/dx^*)]$, where ρ_0^* and x^* are the dimensional density and vertical coordinate of the base flow, respectively. The velocity field $\mathbf{V} = (u, v)$, density ρ , pressure p , and time t are normalized by $\sqrt{gL_m}$, ρ_h , $\rho_h g L_m$ and $\sqrt{L_m/g}$, respectively.

B. Base flow and the primary instability

The dimensionless Euler equations are shown in Appendix A. As a complete description of the perturbation evolution in a RT flow, we assume the initial perturbation to be infinitesimal, and so up to a finite time instant, the perturbation grows exponentially, satisfying the linear stability theory. For a linear primary instability mode with a tangential wave number k , we express the flow field as

$$\bar{\phi}(x, y, t) = \phi_0(x) + \bar{\epsilon}_a \hat{\phi}(x) e^{iky + \bar{\gamma}t} + \text{c.c.}, \quad (1)$$

where $\bar{\phi} = (\bar{\rho}, \bar{u}, \bar{v}, \bar{p})$, $\phi_0 = (\rho_0, 0, 0, p_0)$ with ρ_0 and p_0 denoting the density and pressure of the steady base flow, $\hat{\phi}$ are the eigenfunctions of the primary mode, $\bar{\epsilon}_a \ll 1$ the amplitude, $\bar{\gamma}$ the growth rate, and c.c. the complex conjugate. The mean density and pressure are selected according to Refs. [14–16]

$$\rho_0(x) = [1 - A \tanh(\delta x)] / (1 + A), \quad (2)$$

$$p_0(x) = p_c + \int_{x_c}^x \rho_0(x) dx, \quad (3)$$

where $\delta = A / [2(1 - \sqrt{1 - A^2})]$ is a dimensionless coefficient such that $\min[|\rho_0 / (d\rho_0/dx)|] = 1$ and p_c is a reference pressure at a reference position x_c . δ^{-1} characterizes the thickness of the diffusive density layer. We choose $(p_c, x_c) = (50, -10)$ to be coincide with the previous works [14–16].

Substituting (1) into the governing equations (A1) and retaining the $O(\bar{\epsilon}_a)$ terms, we arrive at a homogenous linear system,

$$\mathbf{E} \hat{\phi}_x - (\mathbf{A} + \bar{\gamma} \mathbf{B}) \hat{\phi} = 0, \quad (4)$$

where the expressions of the coefficient matrices, \mathbf{E} , \mathbf{A} , and \mathbf{B} , can be found in Ref. [16]. The linear system (4) with attenuation boundary conditions, $\hat{\phi}(\pm\infty) \rightarrow 0$, forms an eigenvalue problem, which can be solved by the numerical approach as in Ref. [16]. The analysis in Refs. [14–16] reveals that, an infinite number of primary instability modes are observed when the interface is smeared, and depending on the descend order of their growth rates, they are referred to as modes 1, 2, 3, etc.

C. Secondary instability

As the RT primary instability modes evolve to the nonlinear phase, their amplitudes are likely to saturate, and simultaneously the spike-bubble structure would appear. The latter redistributes the density profile and induces remarkable shears around the spike and bubble boundaries. The nonlinear

structure evolves much gentler, and thus its time scale is lengthened in comparison with its linear counterpart. On the other hand, the simulation of the RT instability in Ref. [16] reveals that small-scale structures emerge in local regions, which grows drastically and eventually leads to turbulent spots. In order to explain and predict the amplification of the small-scale structures, we perform a biglobal instability analysis based on the two-dimensional instantaneous base flow.

As the small-scale structures have much smaller time scales than the nonlinear spike-bubble structure, we freeze the latter at a certain time instant t_0 and study its biglobal instability. The flow field now is decomposed as

$$\phi(x, y, t) = \bar{\phi}(x, y; t_0) + \epsilon_a \tilde{\phi}(x, y) e^{\gamma(t-t_0)} + \text{c.c.}, \quad (5)$$

where $\bar{\phi}$ denote the instantaneous flow field including both the steady base flow ϕ_0 and the nonlinear primary mode, ϵ_a the amplitude of the secondary instability mode, $\gamma = \gamma_r + i\gamma_i$ the complex growth rate with the imaginary part representing its frequency, and $\tilde{\phi}$ its eigenfunction. Note that this mode is the fundamental Floquet mode of a 2D base flow with periodicity in y direction. Substitute of (5) into the Euler equations (A1) with only the $O(\epsilon_a)$ terms being retained, we obtain

$$(\gamma \mathbf{I} + \bar{\mathbf{A}}) \tilde{\phi} + \bar{\mathbf{B}} \frac{\partial \tilde{\phi}}{\partial x} + \bar{\mathbf{C}} \frac{\partial \tilde{\phi}}{\partial y} = 0, \quad (6)$$

where \mathbf{I} is the unit matrix,

$$\bar{\mathbf{A}} = \begin{bmatrix} \bar{u}_x + \bar{v}_y & \bar{\rho}_x & \bar{\rho}_y & 0 \\ \bar{\rho}^{-1}(\bar{u}\bar{u}_x + \bar{v}\bar{u}_y - 1) & \bar{u}_x & \bar{u}_y & 0 \\ \bar{\rho}^{-1}(\bar{u}\bar{v}_x + \bar{v}\bar{v}_y) & \bar{v}_x & \bar{v}_y & 0 \\ 0 & \bar{p}_x & \bar{p}_y & \Gamma(\bar{u}_x + \bar{v}_y) \end{bmatrix},$$

$$\bar{\mathbf{B}} = \begin{pmatrix} \bar{u} & \bar{\rho} & 0 & 0 \\ 0 & \bar{u} & 0 & \bar{\rho}^{-1} \\ 0 & 0 & \bar{u} & 0 \\ 0 & \Gamma\bar{p} & 0 & \bar{u} \end{pmatrix}, \quad \bar{\mathbf{C}} = \begin{pmatrix} \bar{v} & 0 & \bar{\rho} & 0 \\ 0 & \bar{v} & 0 & 0 \\ 0 & 0 & \bar{v} & \bar{\rho}^{-1} \\ 0 & 0 & \Gamma\bar{p} & \bar{v} \end{pmatrix}.$$

(6) is subject to the periodic boundary condition at y boundaries and the attenuation boundary condition at x boundaries.

The base flow $\bar{\phi}$ is obtained from DNS of the evolution of the primary mode, which will be introduced in the next subsection. For a uniform coordinate system, the grid spacings are denoted as Δ_x and Δ_y in the x and y directions, respectively, and the quantities at each grid point (x_i, y_j) are denoted as $\tilde{\phi}_{i,j}$. The linear system (6) is discretized by the fourth-order central difference scheme, which is expressed as

$$\frac{\partial \tilde{\phi}}{\partial x} \Big|_{i,j} = \frac{-\tilde{\phi}_{i+2,j} + 8\tilde{\phi}_{i+1,j} - 8\tilde{\phi}_{i-1,j} + \tilde{\phi}_{i-2,j}}{12\Delta_x} \quad (7)$$

for the x direction and

$$\frac{\partial \tilde{\phi}}{\partial y} \Big|_{i,j} = \frac{-\tilde{\phi}_{i,j+2} + 8\tilde{\phi}_{i,j+1} - 8\tilde{\phi}_{i,j-1} + \tilde{\phi}_{i,j-2}}{12\Delta_y} \quad (8)$$

for the y direction. At the x boundaries, $i = 0, 1, I-1$, and I , we set $\tilde{\phi} = 0$, while at the y boundaries, the subscripts $-2, -1, J+1$, and $J+2$ are replaced by $J-1, J, 0$, and 1 , respectively.

Using the schemes (7) and (8), the linear system (6) is discretized as

$$(\gamma \mathbf{I} + \bar{\mathbf{A}}) \tilde{\phi}_{i,j} - \frac{\bar{\mathbf{B}}}{12\Delta_x} (\tilde{\phi}_{i+2,j} - \tilde{\phi}_{i-2,j}) + \frac{2\bar{\mathbf{B}}}{3\Delta_x} (\tilde{\phi}_{i+1,j} - \tilde{\phi}_{i-1,j}) - \frac{\bar{\mathbf{C}}}{12\Delta_y} (\tilde{\phi}_{i,j+2} - \tilde{\phi}_{i,j-2}) + \frac{2\bar{\mathbf{C}}}{3\Delta_y} (\tilde{\phi}_{i,j+1} - \tilde{\phi}_{i,j-1}) = 0. \quad (9)$$

The discretized system constructs a high-dimensional eigenvalue problem,

$$\mathbf{F} \tilde{\phi} = \gamma \tilde{\phi}, \quad (10)$$

where

$$\tilde{\phi} = (\tilde{\phi}_{0,0}, \tilde{\phi}_{0,1}, \dots, \tilde{\phi}_{0,J}, \tilde{\phi}_{1,0}, \dots, \tilde{\phi}_{I,J})^T,$$

and the coefficient matrix \mathbf{F} is easy to be derived from (9).

Usually, an eigenvalue system can be solved numerically by the QZ method. However, in the present eigenvalue system (10), the dimension of \mathbf{F} is $4(I+1)(J+1) \times 4(I+1)(J+1)$ [both I and J are of $O(100)$ for the resolution requirement], for which the QZ method is not applicable due to its huge computational cost. Therefore, we employ two alternative methods since \mathbf{F} is sparse: (i) the Arnoldi iterative method in the Lapack toolbox in Matlab, which provides a group of eigensolutions, and (ii) the generalized Rayleigh quotient iterative method [30], which only focuses on one eigensolution around the initial value. A brief introduction of method (ii) is shown in Appendix B. Only when the two calculations agree with each other can we confirm our numerical results to be accurate.

D. Direct numerical simulation

In this paper, the DNS approach is employed for two problems: (a) the nonlinear evolution of the primary instability modes and (b) the linear and nonlinear evolution of the secondary instability modes. The DNS code is the same as that used in Ref. [16]. The simulation is performed in a rectangular domain $[\bar{x}_0, \bar{x}_I] \times [\bar{y}_0, \bar{y}_J]$, and the uniform grid points are employed in both the x and y directions. The fifth-order compact upwind finite-difference scheme is employed for the convective terms while the second-order Runge-Kutta scheme for time advancing. The periodic boundary conditions are employed in the y direction, while the attenuation conditions in the x direction.

For problem (a), we first consider a single-mode configuration by introducing a small density perturbation with only one wave number in the direction tangential to the interface (following Ref. [16]),

$$(\bar{\rho}, \bar{u}, \bar{v}, \bar{p})(x, y, 0) = (\rho_0 + \bar{\epsilon}_a f(x) \cos(ky), 0, 0, p_0), \quad (11)$$

where $\bar{\epsilon}_a$ is the initial amplitude and $f(x)$ is the initial distribution of the density perturbation. Note that the results for a multimode configuration will be demonstrated in Sec. IV. Here we choose the parameters from case 3 of Ref. [16], i.e., $A = 0.4$, $k = 4.672$, $\bar{\epsilon}_a = 0.005$, and $f(x) = e^{-x^2}$. The computational domain for DNS is selected as $\bar{x}_0 = -10$, $\bar{x}_I = 10$, $\bar{y}_0 = 0$ and $\bar{y}_J = 2\pi/k$, and 2001×121

grid points are used. It is seen from Fig. 9 of Ref. [16] that the spike-bubble structure has already been formed at $t = 7$, and the secondary instability modes analysis will be performed from this time instant.

For problem (b), we start the simulation from a chosen time instant $t = t_0$, and the initial flow $\phi(x, y, t_0)$ is a superposition of a base flow $\bar{\phi}(x, y, t_0)$ calculated from step (a) and an infinitesimal secondary mode from the biglobal analysis. For the secondary mode, we choose $\epsilon_a = 10^{-6}$ and $t_0 = 7$ for representative demonstration. The computational domain in x direction is shortened to $\bar{x}_0 = -5$ and $\bar{x}_l = 5$, but that in y direction remains the same as in problem (a). In order to capture the evolution of the small-scale structures, we increase the number of grid points in y direction to 481. Good resolution has been confirmed as shown in Appendix C.

III. NUMERICAL RESULTS FOR A SINGLE-MODE CONFIGURATION

A. Nonlinear evolution of the primary instability

For the parameters shown in problem (a) of Sec. IID, the detailed DNS results of the formation and evolution of the most unstable primary mode (mode 1) can be seen in Ref. [16]. For demonstration purpose, the computational domain of the simulation includes only one wavelength in the direction tangential to the interface, which is also referred to as the single-mode simulation. The secondary instability analysis (SIA) in this paper is based on this flow field. It has to be stressed that our analysis is also applicable to the flow field of multimode simulations, and can be extended to the three-dimensional configurations by taking into account the derivative with respect to the transverse direction. It was found from Fig. 11 of that paper that the primary mode becomes nonlinear at around $t = 4$, after which the spike and bubble lengths grow linearly with t until $t \approx 10$. This was recognized as an asymptotic growth in the nonlinear state [1,6,18]. Note that during this time interval, $4 < t < 10$, the amplitude of the nonlinear primary mode, shown in Fig. 4(c) of Ref. [16], deviates from the exponential growth remarkably and tends to saturate, and its amplitude is amplified from $O(0.1)$ to $O(1)$. On the other hand, for $t < 4$, the linear primary mode is amplified from $O(10^{-6})$ to $O(0.1)$, implying a much smaller timescale. The timescale of the secondary mode, as will be shown numerically in the next subsection, is comparably smaller than that of the linear primary mode due to its higher growth rate and oscillatory manner. The implication is that in the nonlinear saturation phase, the secondary mode has a much smaller timescale than the nonlinear primary mode, confirming the treatment that freezes the nonlinear bubble-spike structure to be reasonable. In later phases, $t > 10$, the spikes and bubbles grow quadratically with t . Figure 1(a) displays the contours of the density $\bar{\rho}$ at three representative time instants in the nonlinear saturation phase, $t = 7, 8$, and 9. The development of the spike-bubble structure around the interface can be seen clearly, and the small-scale perturbations have not appeared yet. The velocity vector fields at the three t s are shown in Fig. 1(b). As the heavy fluids in the spike head penetrate into the light fluids, the ambient light fluids move laterally and toward the opposite direction,

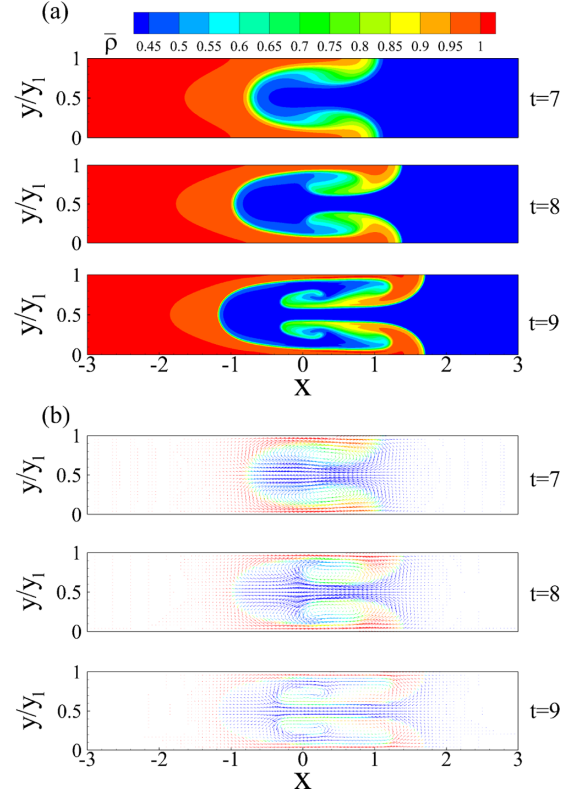


FIG. 1. Contours of the density $\bar{\rho}$ (a) and velocity vector (b) for $t = 7, 8$, and 9.

which induces a remarkable shear at the interface. Figure 2(a) plots the contours of the vorticity $\bar{\Omega} \equiv \bar{v}_x - \bar{u}_y$ at these time instants. The vorticity field at each t exhibits a strip of peak or valley on the each side of the spike head, which becomes elongated with a curved tail as the spike grows. This indicates a large gradient of velocity in y direction. Around the peaking strips of the vorticity field, the fluids move tangentially to the strips, implying a strong-shear manner. As illustrated in Refs. [3,31], the production of the vorticity is linked to the misalignment of the pressure gradient with the density interface via

$$\frac{D\bar{\Omega}}{Dt} = \bar{\rho}^{-2} \nabla \bar{\rho} \times \nabla \bar{p}. \quad (12)$$

The term on the right-hand side is referred to as the baroclinic torque, whose contours for the three t s are shown in Fig. 2(b). It needs to be stressed that $\bar{\rho}$ and \bar{p} are the instantaneous flow including both the steady base flow, (ρ_0, p_0) , and the primary mode. The former does not have baroclinic torque because ρ_0 and p_0 are not misaligned, whereas the latter induces a nonzero baroclinic torque, which increases with time due to the linear instability regime. The peak and valley appear at each side of the spike head, indicating a progressively increasing vorticity appearing at the right side of the spike-bubble structure. Such a stretching leads to the growth of the spike length with time.

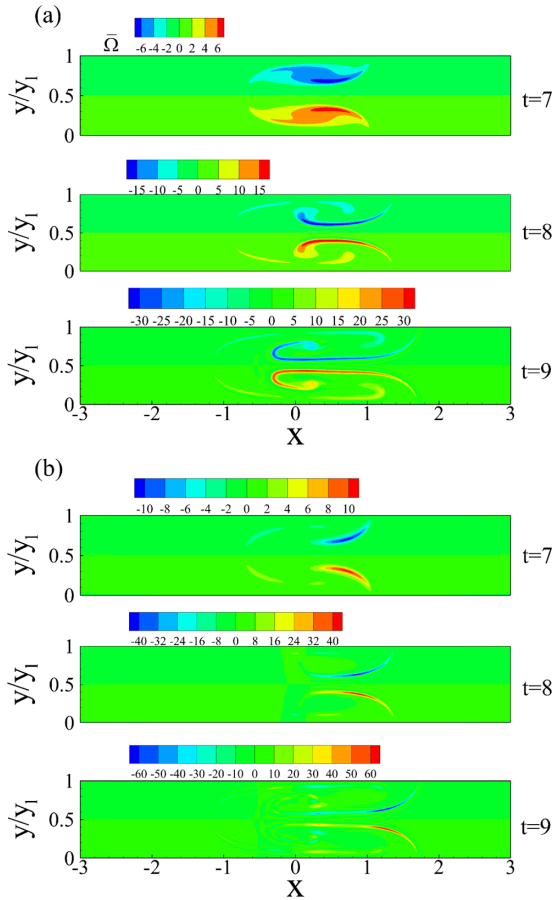


FIG. 2. Contours of the vorticity $\bar{\Omega}$ (a) and baroclinic torque (b) for $t = 7, 8,$ and 9 .

B. Secondary instability analysis

Based on the flow field $\bar{\phi}$ at $t_0 = 7, 8,$ and 9 , we perform the biglobal instability analysis using both the Arnoldi and Rayleigh quotient iterative methods. The most unstable eight eigenvalues $\gamma = \gamma_r + i\gamma_i$ of the secondary instability modes for each t_0 are shown in Fig. 3. The eigenvalues appear in pairs, with the same growth rate γ_r but opposite frequencies γ_i . For $\gamma_i \geq 0$, the secondary modes are referred to as modes S1, S2, S3, and S4 according to the descend order of their growth

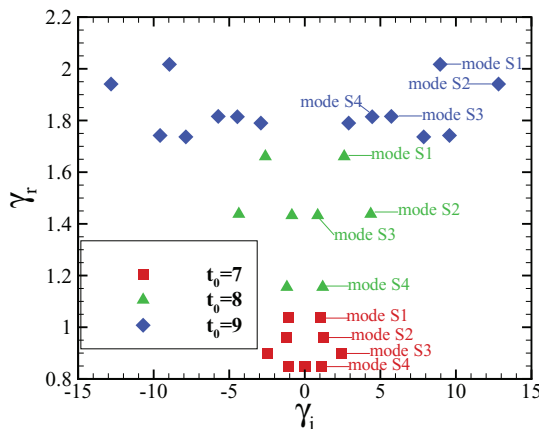


FIG. 3. Complex growth rate γ of the secondary instability modes.

TABLE I. Parameters of multiple secondary instability modes at different time instants.

Time	Mode	γ	Type
$t_0 = 7$	S1	$1.0361 + 1.0648 i$	Sinusous
$t_0 = 7$	S2	$0.9599 + 1.2171 i$	Varicose
$t_0 = 7$	S3	$0.8987 + 2.4359 i$	Sinusous
$t_0 = 7$	S4	$0.8477 + 1.0754 i$	Sinusous
$t_0 = 8$	S1	$1.6607 + 2.6088 i$	Sinusous
$t_0 = 8$	S2	$1.4380 + 4.3644 i$	Sinusous
$t_0 = 8$	S3	$1.4330 + 0.8540 i$	Sinusous
$t_0 = 8$	S4	$1.1554 + 1.1853 i$	Varicose
$t_0 = 9$	S1	$2.0172 + 8.9581 i$	Sinusous
$t_0 = 9$	S2	$1.9410 + 12.821 i$	Sinusous
$t_0 = 9$	S3	$1.8158 + 5.7284 i$	Sinusous
$t_0 = 9$	S4	$1.8145 + 4.4612 i$	Sinusous

rates. Note that there also exist eigenvalues with $\gamma_i = 0$, but they are of less interest because their growth rates are smaller. The eigenvalues and the symmetric types of the first four modes for the selected t_0 s are listed in Table I. For a sinusous mode, $\bar{u}, \bar{\rho},$ and \bar{p} are antisymmetric along the centerline, $y = y_l/2$, but \bar{v} is symmetric. The opposite is true for a varicose mode. As the primary perturbation develops (t_0 increases), the secondary instability modes become more unstable and the frequency of the most unstable mode becomes higher. Note that the linear growth rate of the primary instability must be less than unity, as Ref. [15] indicates, but the secondary instability does not have this limitation. At the selected time instants, the primary instability mode almost saturates, and such high growth rates ensure that the small-scale perturbations emerge and grow rapidly, which would eventually lead to turbulent mixing. For $t_0 = 7$, the eigenfunctions $\bar{\rho}, \bar{u},$ and \bar{v} of the most unstable mode, mode S1, are shown in Fig. 4, for which the complex growth rate γ is $1.0361 + 1.0648i$. All the eigenfuntions are normalized such that $\max_{x,y} |\bar{u}| = 1$. $\bar{\rho}$ and \bar{u} are antisymmetric along the centerline $y = y_l/2$, while \bar{v} is symmetric, indicating a sinusous nature. The norm of the perturbation velocity $|\bar{u}|$ peaks in a pair of narrow-strip ranges, $-0.2 < x < 0.6$ and $y/y_l \approx 0.5 \pm 0.15$, which are at the boundary of the bubble penetrating into the heavy

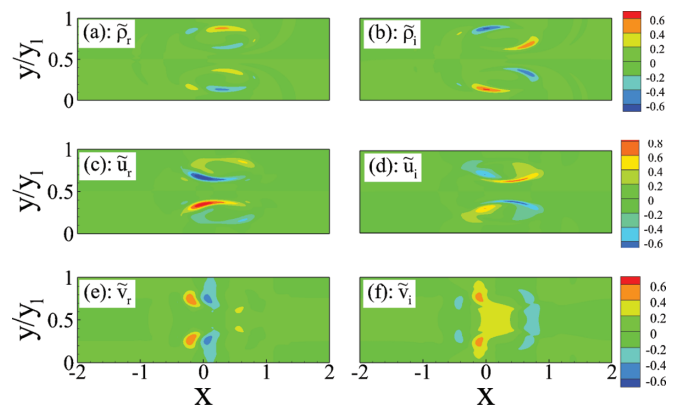


FIG. 4. Eigenfunctions $\bar{\rho}, \bar{u},$ and \bar{v} of mode S1 for $t_0 = 7$. Left column: real part; right column: imaginary part.

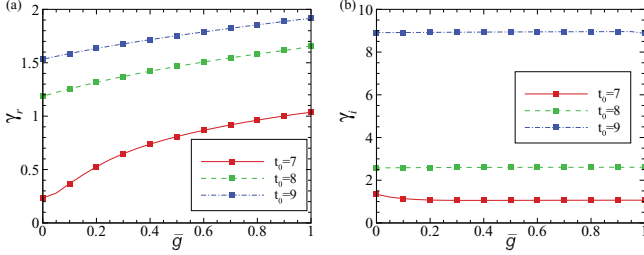


FIG. 5. Variation of the growth rate (a) and the frequency (b) with the acceleration \bar{g} .

fluid, as Fig. 1(a) indicates. Additionally, there exist a pair of mild peaks in the narrow strips of $-0.2 < x < 0.8$ and $y/y_l \approx 0.5 \pm 0.35$, which are at the boundary of the spike penetrating to the light fluid. The vorticity of the base flow, shown in Fig. 2(a), also exhibits peaks at these strip regions, indicating that the velocity gradient plays an important role in the formation of this eigenprofile. Such a shear-driven instability indicates a KH regime. Additionally, the acceleration may also act as a factor to drive secondary instability, which is of the RT regime. In order to show the impact of the acceleration on the secondary instability, we compare the numerical results obtained by the biglobal analysis with and without the acceleration term. This is done by reexpress $\{\bar{A}\}_{21}$ in (6) by $\bar{\rho}^{-1}(\bar{u}\bar{u}_x + \bar{v}\bar{v}_y - \bar{g})$, where \bar{g} represents the acceleration. As \bar{g} reduces from 1 to 0, the impact of the acceleration on the secondary instability is removed gradually. The variations of γ_r and γ_i with \bar{g} for $t_0 = 7$ are shown as the red curves in Figs. 5(a) and 5(b), respectively. Reducing \bar{g} leads to a reduction of the growth rate γ_r , and the reduction rate, defined as $1 - \gamma_{r,\bar{g}=0}/\gamma_{r,\bar{g}=1}$, is around 0.77. The implication is that the growth rate of the secondary instability mode is affected by both the KH and RT regimes, and the latter is dominant at this t_0 . On the other hand, the frequency γ_i stays almost constantly as \bar{g} varies, implying that the oscillation of the secondary instability mode is contributed only by the shear (KH) effect. We have also compared the eigenfunctions obtained by different \bar{g} , and only quantitative differences are observed (not shown).

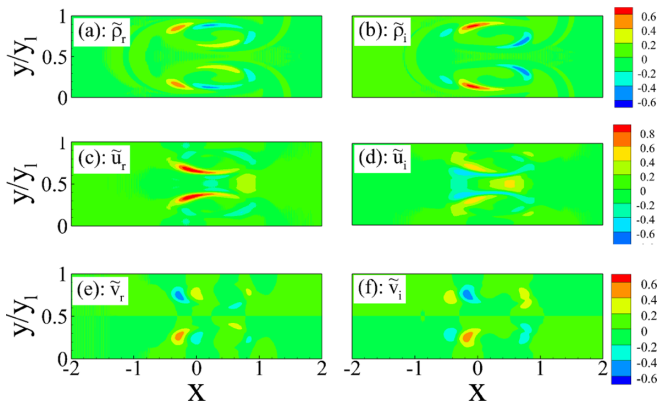


FIG. 6. Eigenfunctions $\tilde{\rho}$, \tilde{u} , and \tilde{v} of mode S2 for $t_0 = 7$. Left column: real part; right column: imaginary part.

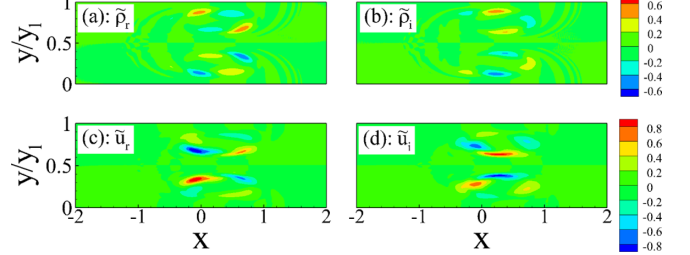


FIG. 7. Eigenfunctions $\tilde{\rho}$ and \tilde{u} of mode S3 for $t_0 = 7$. Left column: real part; right column: imaginary part.

Figure 6 shows the eigenfunctions of mode S2. The peaks of the eigenfunctions \tilde{u} and $\tilde{\rho}$ are locating at almost the same strip regions as those of mode S1, but the symmetric feature is on the opposite direction since this is a varicose mode. Figure 7 shows the eigenfunctions $\tilde{\rho}$ and \tilde{u} of the sinuous mode S3. Being different from mode S1, each peaking strip breaks into two segments of peaks with opposite phases. This is a reminiscent of the observation of the RT primary instability with a smeared interface: The higher-order mode always exhibits more local extremes than the lower one, which was explained by a WKB solution with two turning points in Ref. [15]. Therefore, the emergence of mode S3 is linked to the diffuse interface effect. Figure 8 and Figure 9 plot the eigenfunctions of mode S1 for $t_0 = 8$ and 9, respectively. As the vorticity of the base flow stretches, the peaking strips of $|\tilde{u}|$ are elongated for $t_0 = 8$, but the eigenprofiles for $t_0 = 9$ exhibit a number of local extremes with small length scales. Such small-scale perturbations are linked to its high-frequency nature as shown in Fig. 3. The green and blue curves in Fig. 5 show the variations of γ with \bar{g} for $t_0 = 8$ and 9, respectively. As the spike-bubble structure develops, the shear rate of the base flow becomes stronger, and $1 - \gamma_{r,\bar{g}=0}/\gamma_{r,\bar{g}=1}$ is reduced to about 0.20 for $t_0 = 9$. The implication is that as time advances, the KH instability regime plays an increasingly important role on the formation of the secondary instability modes.

C. Evolution of the secondary instability modes

In order to confirm the accuracy of the SIA and further reveal how the secondary instability modes lead to turbulent mixing, we calculate their evolution by DNS from a selected time instant t_0 . The base flow of the initial perturbation (5) is from the simulation of the primary-mode evolution, while the perturbation is from the SIA in the previous subsection. Two

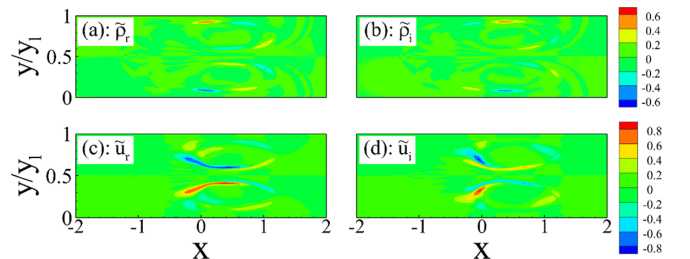


FIG. 8. Eigenfunctions $\tilde{\rho}$ and \tilde{u} of mode S1 for $t_0 = 8$. Left column: real part; right column: imaginary part.

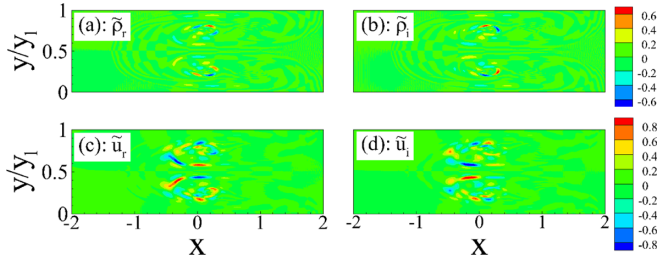


FIG. 9. Eigenfunctions $\tilde{\rho}$ and \tilde{u} of mode S1 for $t_0 = 9$. Left column: real part; right column: imaginary part.

case studies are considered, whose key parameters are listed in Table II.

The secondary instability mode at each time instant can be obtained by

$$\tilde{u}_1(x, y, t) = u(x, y, t) - \bar{u}(x, y, t), \quad (13)$$

where u denotes the instantaneous velocity and \bar{u} the velocity for the evolution of the primary perturbation. Its amplitude is defined as

$$A_{u,DNS}(t) = \max_{x,y}\{|\tilde{u}_1|\}, \quad (14)$$

and the location corresponding to the peak of $|\tilde{u}_1|$ is denoted as (x_m, y_m) . Due to the symmetric nature of the perturbation field, there are two peaks in the $|\tilde{u}_1|$ profile. Therefore, we only choose the one for which $y_m/y_l \leq 0.5$.

The red curve in Fig. 10 shows the evolution of $A_{u,DNS}(t)$ for case 1, which is piecewisely growing. The curve is compared with the linear prediction based on the growth rate from the SIA (green curve),

$$A_{u,LINEAR} = \epsilon_a e^{\gamma(t-t_0)} + c.c., \quad (15)$$

where γ is the growth rate of the introduced secondary instability mode. According to the linear prediction, the perturbation grows exponentially with a sinusoidal oscillation, whose period is $2\pi/|\gamma_i|$. The two curves agree precisely for $t - t_0 < 0.7$, and the peaking location of $|\tilde{u}_1|$, as shown in Fig. 11, varies gently around $(x_m, y_m/y_l) = (-0.05, 0.35)$, which agrees with the peaking location of the mode S1 eigenprofile for $t_0 = 7$. These features indicate that mode S1 dominates the perturbation field before $t - t_0 = 0.7$, and the accuracy of the SIA is confirmed. The gentle change of x_m and y_m is due to the relatively slow development of the primary mode, which leads to a slow variation of the base flow for the SIA. After $t - t_0 = 0.7$, $A_{u,DNS}$ undergoes a much greater growth, and the perturbation peak is suddenly jumped to $(x_m, y_m/y_l) \approx (0.65, 0.4)$. This position undergoes only mild change in the time interval $t - t_0 \in (0.7, 1.6)$, in which another mode dominates the perturbation field. From $t - t_0 = 1.6$, $A_{u,DNS}$ starts to show a new growth again, and the perturbation

TABLE II. Parameters for DNS case studies.

Case	t_0	Mode	ϵ_a	γ
1	7	S1	10^{-6}	$1.0361 + 1.0648 i$
2	7	S2	10^{-6}	$0.9599 + 1.2171 i$

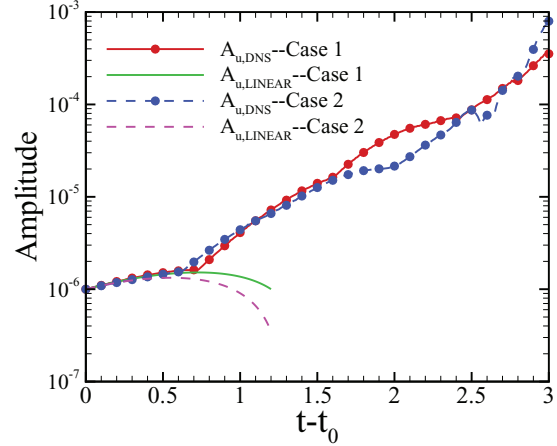


FIG. 10. Amplitude evolutions for case 1 and case 2.

bation peak suddenly changes to $(x_m, y_m/y_l) \approx (-0.05, 0.4)$. After that the x_m position moves toward the heavier fluid direction successively, until $t - t_0 \approx 2.4$.

Figure 12 shows the contours of the eigenfunction normalized by the maximum of its norm, $\tilde{u} \equiv \tilde{u}_1/\max_{x,y}\{|\tilde{u}_1|\}$, at different time for case 1. The perturbation velocity \tilde{u} is antisymmetric about $y = y_l/2$, and the initial peak is located in a pair of narrow-strip regions with $-0.2 < x < 0.6$ and $y/y_l \approx 0.5 \pm 0.15$. As time advances, the peaking strips become thinner and are stretching around the high-shear region, which eventually break into small structures after $t > 9.5$. Subsequently, the perturbation field is not exactly antisymmetric any more, which is caused by the accumulation of the numerical noises. Although they are initially tiny, they can be amplified substantially due to the unstable nature of the RT flow. This also explains the abnormal change of the peak position of the perturbation after $t - t_0 > 2.4$ in Fig. 11.

Figure 13 compares the energy spectra of v around $x = 0$ among different time instants. It is seen that as t advances from 8 to 10, the energy of the small-scale (high-wave-number) perturbations increases remarkably, due to the growth of the secondary instability modes. At $t = 10$, the

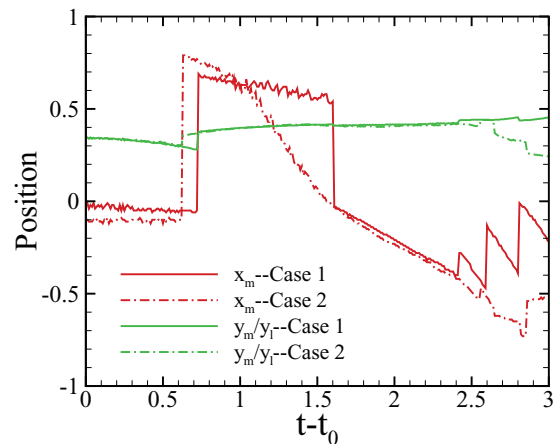


FIG. 11. The positions of the perturbation peak for case 1 and case 2.

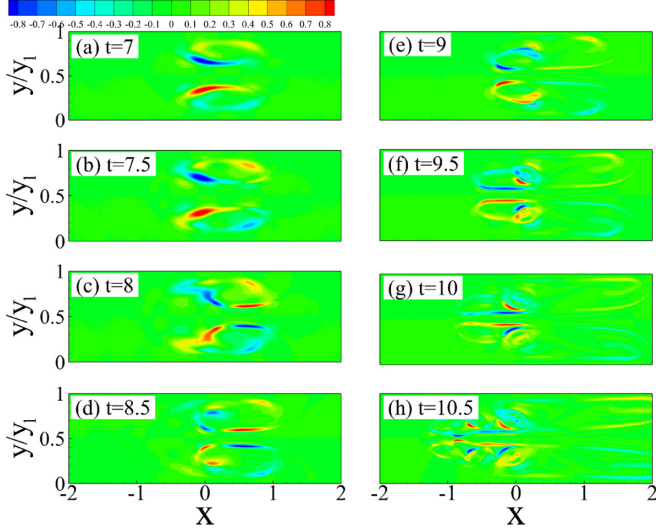


FIG. 12. Contours of the perturbation \tilde{u} at representative time instants for case 1.

scaling law of the 2D turbulence, $E(k) \sim k^{-8/3}$, is reached in the interval $k \in (3, 25)$, and such a scaling law persists to later time instants, e.g., $t = 12$. These observations show a transitional trend from laminar to turbulent mixing, although the fully turbulent state may not be reached because the single-mode configuration limits the development of the perturbations with larger length scales than the domain size.

The blue and pink curves in Fig. 10 represent respectively the perturbation amplitude $A_{u,DNS}$ and $A_{u,LINEAR}$ for case 2, for which the initially introduced secondary mode is varicose. The agreement is good for $t - t_0 < 0.6$, which is slightly shorter than that for case 1. The time interval for the second segment of growth is until $t - t_0 \approx 2.0$, and at this time, the amplitude for case 2 is much smaller than that for case 1. At latter time instants, the amplitudes of the two cases become comparable. The peaking locations for case 2 follow the similar trend as those for case 1, as Fig. 11 indicates. Figure 14 further shows the contours of \tilde{u} at different t s for

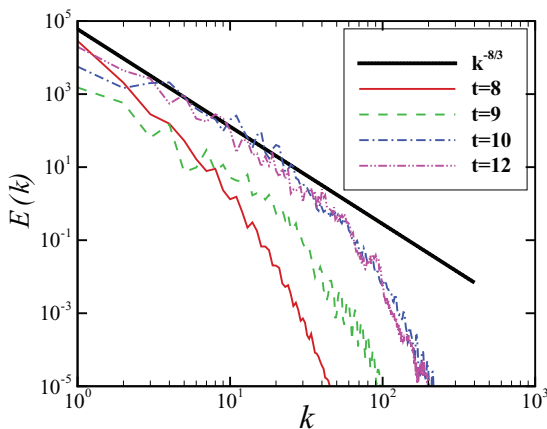


FIG. 13. Comparison of the energy spectra $E(k)$ among different time instants for case 1.

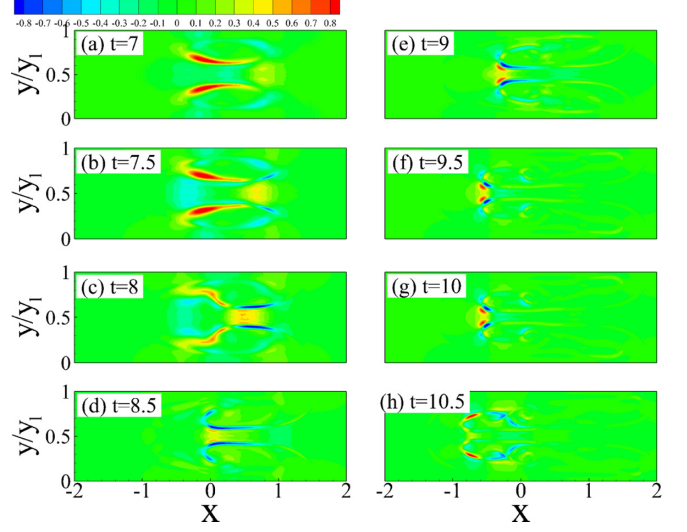


FIG. 14. Contours of the perturbation \tilde{u} at representative time instants for case 2.

case 2. The evolution of the symmetric-type perturbation from longitudinal strips to short scales is clearly exhibited.

IV. APPLICATION OF THE SIA TO A MULTIMODE CONFIGURATION

Differing from Sec. III, in this section, we will focus on a multimode configuration. Now the initial flow field (11) is changed to

$$\left(\rho_0 + \bar{\epsilon}_a f(x) \left[\cos(ky) + \cos\left(\frac{ky}{2}\right) \right], 0, 0, p_0 \right), \quad (16)$$

where all the parameters stay the same as in Sec. III. The computational domain in the y direction is doubled, $\bar{y}_l = 4\pi/k \approx 2.69$, and the number of grid points are changed to 2001×241 .

Comparing the initial perturbations (16) and (11), we find that the effective amplitude of the multimode configuration is higher, and so the nonlinear saturation phase is arrived a bit earlier. Figure 15 shows the contours of the density subject to the initial perturbation (16) at three representative time instants, which are earlier than those in Fig. 1(a). Because of the interaction of the two modes with different wave numbers,

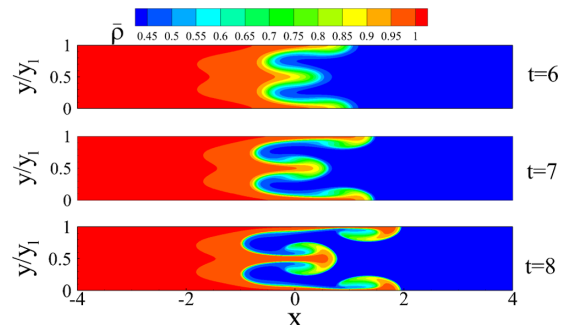


FIG. 15. Contours of the density $\bar{\rho}$ for the multimode configuration.

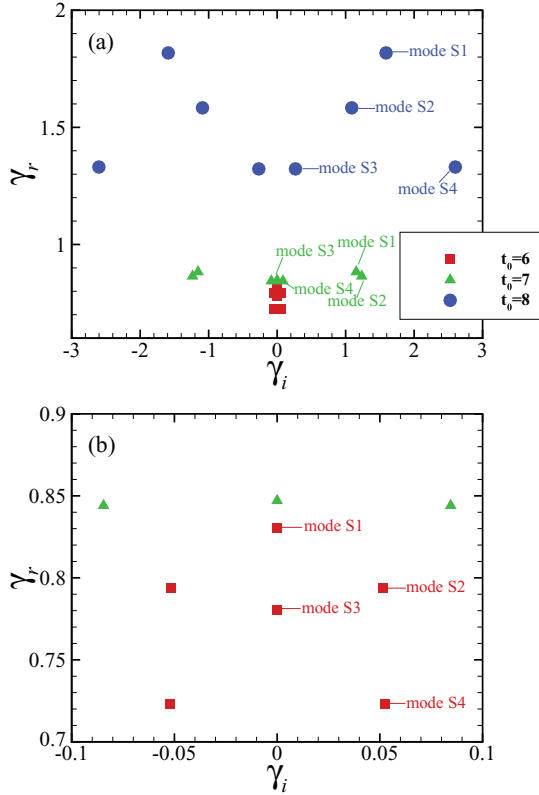


FIG. 16. Complex growth rate γ of the secondary instability modes for a multimode configuration, where (b) is a zoom-in plot of (a).

two spikes with different lengths are observed. As the spikes stretch, the shear rates of the flow are increasing, leading to the emergence of KH-type secondary instability. Using the same analysis approach as in Sec. III, we obtain the eigenvalues of the secondary instability modes in the three time instants, as shown in Fig. 16. The overall trend is the same as that in Sec. III. As time advances, both the growth rates and the oscillation frequencies become higher, and the sinuous modes are more unstable.

The eigenfunctions of the most unstable secondary instability mode, mode S1, for the three representative time instants are plotted in Fig. 17. The peaks of the eigenfunctions appear at the edge of the spikes overall, in agreement with the high-shear regions. It is confirmed that the SIA developed in this paper is easy to be extended to more complicated configurations.

V. DISCUSSION

Admittedly, the role of the KH instability on the generation of the small-scale (secondary) perturbations is well known for decades. However, we argue that the novelty of this study is the development of a quantitative means to identify the dominant factor contributing to the secondary instability. From the analysis in Sec. III B, we have shown a transition of the dominant factor from acceleration (RT regime) to shear (KH regime) during the nonlinear saturation phase, and in this section, using this efficient tool, we will clarify another

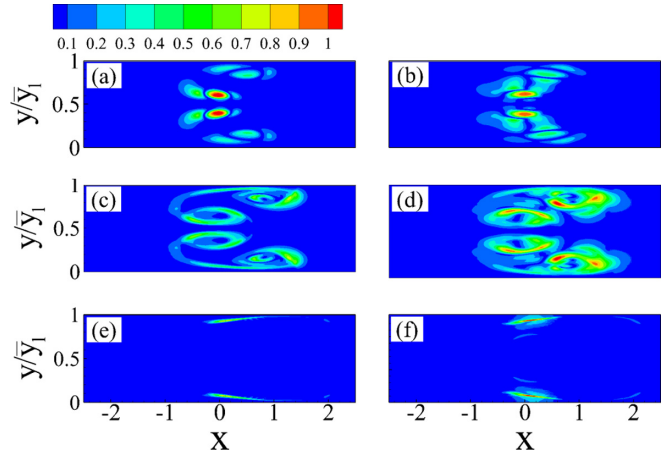


FIG. 17. Eigenfunctions of mode S1 for $t = 6$ [(a) and (b)], 7 [(c) and (d)], and 8 [(e) and (f)], where the left and right columns are for $|\hat{\rho}|$ and $|\hat{u}|$, respectively.

still-obscure issue, i.e., the relation between the secondary instability of the bubble-spike structure and the instability of a rising bubble.

An early experimental observation by Davies and Taylor [27] showed that for a gas bubble rising vertically in extended liquids or liquid tube, the bubble would approach a constant curvature and rise in a constant speed in the long-time limit. Such a setup is equivalent to the growth of bubbles in a RT flow with the Atwood number $A \approx 1$, and the observation time period is within the nonlinear saturation phase. A subsequent theoretical study [28] presented a family of steady solutions for 2D bubbles, and the sliding of the surrounding liquids are unlikely to induce KH instability. Based on the group theory approach, Abarzhi [29] confirmed that only a small portion of the possible solutions are stable, and the prediction of the 2D bubble velocity agrees with that in Ref. [28]. The bubble velocity for an arbitrary density ratio ($A \in (0, 1)$), a more generic situation, was presented by Goncharov [6], which agrees with Abarzhi’s result when $A = 1$. The growth of spikes in a RT flow was later predicted theoretically by Duchemin *et al.* [32]. A recent review of the bubble and spike dynamics can be found in Ref. [33].

In fact, whether the secondary instability of the RT flow is purely driven by the rising-bubble effect is still an open question. On the one hand, no experiment on rising bubbles has provided sufficient evidence to support the KH instability, which may be attributed to the limitation of observing time (restricted by the finite-length nature of the vertical tube). On the other hand, in RT unstable flows, we do observe the emergence of small-scale perturbations, although there is a combined effect with the spikes penetrating into the light fluid. It is seen from Figs. 6, 7, 8, and 9 that the peaks of the eigenfunctions of the secondary modes are mainly located at the side boundaries of the bubbles and spikes. If the spikes in the RT flow are eliminated by a proper artificial filtering, then its SIA could reflect the instability of the rising bubble. Figure 18 shows the temporal evolution of the bubble front for the single-mode case in Sec. III. The bubble approaches a constant-speed state from $t \approx 4$, and as shown in Fig. 11 of Ref. [16], a quadratic growth is arrived after $t \approx 10$. Thus,

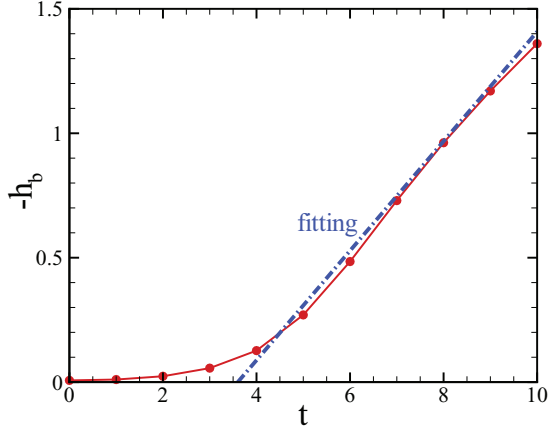


FIG. 18. Temporal evolution of the bubble front position $-h_b$.

three representative time instants, $t_0 = 6, 7$, and 8 , are chosen for the filtered SIA. Because the spikes are developing in the region of $x > 0$, the simplest treatment for the filtering is to cut off the base flow as used in Sec. III from $x = 0$, and perform SIA in the domain $x \in [-2, 0]$ and $y \in [0, 2\pi/k]$. Note that $x = -2$ is sufficient to include the bubble front in these time instants.

The eigenvalues of the SIA of the filtered bubbles for $t_0 = 6, 7$, and 8 are plotted in Fig. 19, where the most unstable sinuous and varicose modes are denoted by BS1 and BV1, respectively. As time advances, mode BS1 becomes less unstable, whereas the growth rates of mode BV1 stay almost unchanged. Remarkably, for each time instant, the eigenvalues γ of both BS1 and BV1 are pure real, in contrast to Fig. 3. The implication is that the unstable modes are growing exponentially in time without exhibiting an oscillatory nature, which, in general, is closer to the RT nature. In order to confirm this, we show the growth rate γ_r as the acceleration decreases gradually from 1 to 0, as shown in Fig. 20. Note that for $t_0 = 8$, the continuation for BS1 shown in Fig. 20(b) is stopped at $\bar{g} = 0.4$, because the base flow is contaminated by the small-scale perturbations and the spike to the light-fluid

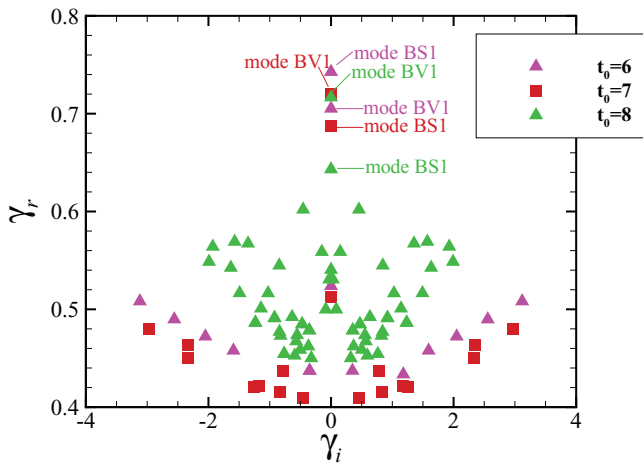


FIG. 19. Complex growth rate γ of the secondary instability for filtered bubbles.

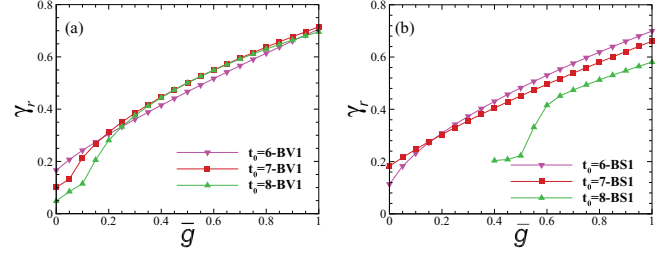


FIG. 20. Variation of the growth rate with the acceleration \bar{g} for modes BV1 (a) and BS1 (b).

side as time advances. However, the overall trend is well captured. For each case, the growth rate reduces over 70% as \bar{g} decreases from 1 to 0, implying the dominant role of the acceleration. This confirms that the instability of the rising bubble is driven by the RT regime, instead of the KH regime.

Comparing Figs. 19 and 3, we find that for the same time instant, the growth rates of the rising bubble (filtered RT bubble) are always smaller than those of the secondary instability of the RT spike-bubble structure. At $t_0 = 7$, the differences of the most unstable sinuous and varicose modes between the secondary instability of the RT bubble and rising bubble are only 33% and 24%, respectively, confirming that the early-time secondary instability of the spike-bubble structure is driven by the RT regime of the rising-bubble effect. At a later time instant, $t_0 = 8$, the differences of the sinuous and varicose modes become 61% and 38%, respectively, which confirms that the KH regime becomes more important as time advances, especially for the sinuous modes. It is also seen that when the RT regime is dominant, the frequency of the secondary mode, measured by γ_i , is relatively lower.

Through the analysis in this section, the mechanism of the secondary instability of the spike-bubble structure of the nonlinear RT flow is clearer. At early time, the secondary instability is dominated by the RT regime, which is due to the rising-bubble effect. As time advances, the spike stretches at a greater speed than the bubble does, strengthening the shear rates of the spike edge. Such a behavior indicates that the KH regime, with higher growth rates and oscillatory frequencies, becomes dominant in later time, but the rising-bubble effect on the late-time growth of the secondary instabilities is quite limited.

VI. CONCLUSION

In order to fully understand the laminar-turbulent transition mechanism of a RT flow with a diffuse interface, a series of previous works [14–16] have studied the excitation and evolution of the multiple RT primary modes. Although it is well accepted that the excitation and rapid amplification of the small-scale structures in the nonlinear saturation phase are driven by the KH secondary-instability regime, one still lacks a comprehensive understanding of this regime and a quantitative means to describe the instability nature. The present paper focuses on this issue by performing the biglobal stability analysis, using Arnoldi and generalized Rayleigh quotient iteration methods. A number of secondary modes are calculated, which are of either sinuous or varicose type, and the

sinuous ones are found to be more unstable overall. The eigenfunctions of the higher-order modes usually have more local extremes, indicating a diffuse-interface effect. The growth rates of the secondary modes are generally complex, with their imaginary parts representing the oscillating frequencies, which is different from that of the primary modes. As the spike-bubble structure develops, both the growth rates and frequencies become higher, implying that more small-scale perturbations are likely to appear and grow rapidly at later time instants. The local peaks of the eigenfunctions of the secondary instability modes are relevant to either the shear of the base flow or the acceleration, indicating that the instability is driven by both the KH and the RT regimes. This is in contrast to the traditional viewpoint that the secondary instability is driven by merely the KH regime [1–3,25,26]. The frequencies of the secondary modes are determined by the KH regime, while both regimes contribute to their growth rates. It is proven that the KH regime, associated with the high shear of the spike edge, plays a dominant role at later time, whereas the RT regime, induced by the rising-bubble effect, dominates the early-time secondary instability. Additionally, we have confirmed the accuracy of the secondary-instability analysis by performing direct numerical simulations of the evolution of the secondary modes, and their late-time evolution to small-scale structures is also exhibited.

The secondary-instability-analysis approach developed in this paper is applicable for both single-mode and multimode primary perturbations, as confirmed in Sec. IV, and the overall trend of the variation of the eigenvalues with time for the multimode configuration is quite similar to that for the single-mode configuration. Note that our analysis approach can also be extended to three-dimensional configurations, but another coordinate z that is perpendicular to both x and y has to be added to the system.

ACKNOWLEDGMENTS

This research is supported by NSFC (Grants No. 11772224, No. 11871114, and No. 11775030).

APPENDIX A: EULER EQUATIONS

For a two-dimensional perfect-gas inviscid fluid, the dimensionless governing equations are

$$\left. \begin{aligned} \rho_t + (\rho u)_x + (\rho v)_y &= 0, \\ (\rho u)_t + (\rho uu)_x + (\rho uv)_y &= -p_x + \rho, \\ (\rho v)_t + (\rho uv)_x + (\rho vv)_y &= -p_y, \\ p_t + up_x + vp_y + \Gamma p(u_x + v_y) &= 0, \end{aligned} \right\}, \quad (\text{A1})$$

where $\Gamma = 5/3$ is the adiabatic exponent.

APPENDIX B: BRIEF INTRODUCTION OF THE RAYLEIGH QUOTIENT ITERATIVE METHOD

Consider a generalized eigenvalue problem

$$\mathbf{A}_0 \psi = \hat{\gamma} \mathbf{B}_0 \psi, \quad (\text{B1})$$

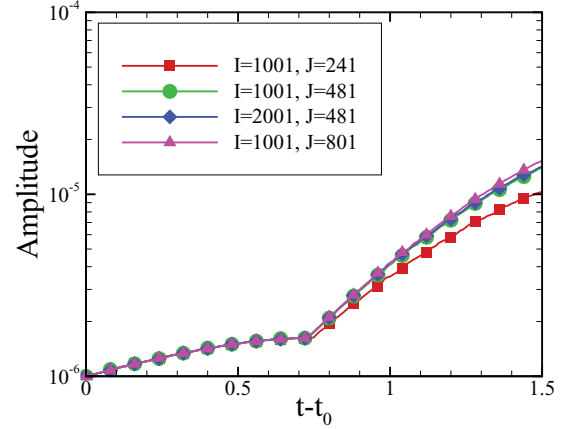


FIG. 21. Amplitude evolution under different mesh systems for case 1.

where the coefficient matrices \mathbf{A}_0 and \mathbf{B}_0 are known, $\hat{\gamma}$ is the eigenvalue and ψ is the eigenvector. We solve the eigenvalue problem by the following steps.

(i) Given an initial guess for the eigenvalue and eigenvector, denoting as $\hat{\gamma}_k$ and ψ^k , respectively. For the first step, $k = 0$.

(ii) Update ψ . Solve $\bar{\psi}^{k+1}$ from the linear system

$$(\mathbf{A}_0 - \hat{\gamma}_k \mathbf{B}_0) \bar{\psi}^{k+1} = \mathbf{B}_0 \psi^k, \quad (\text{B2})$$

and then renormalize $\bar{\psi}^{k+1}$ as

$$\psi^{k+1} = \frac{\bar{\psi}^{k+1}}{\max(\bar{\psi}^{k+1})}. \quad (\text{B3})$$

(iii) Update $\hat{\gamma}$ according to

$$\hat{\gamma}_{k+1} = \frac{\langle \mathbf{H} \mathbf{B}_0 \psi^{k+1}, \mathbf{A}_0 \psi^{k+1} \rangle}{\langle \mathbf{H} \mathbf{B}_0 \psi^{k+1}, \mathbf{B}_0 \psi^{k+1} \rangle}, \quad (\text{B4})$$

where \mathbf{H} is an arbitrary Hermitian positive definite matrix and here is taken to be the unit matrix, and the angle brackets denote the inner product.

(iv) Replace k by $k + 1$ and repeat steps 2 to 3 until $\hat{\gamma}$ converges.

In the calculations, the initial eigenvalue $\hat{\gamma}_0$ is set from the solutions obtained by the Arnoldi iterative method, and ψ^0 is given by a random function. If the eigenvalues obtained by the two methods agree, then we affirm that our numerical results are reliable.

APPENDIX C: RESOLUTION STUDY FOR THE SIMULATION OF THE EVOLUTION OF THE SECONDARY INSTABILITY MODES

Figure 21 compares the amplitude evolution of the secondary instability mode for case 1 of Table II among different mesh systems. The results for $(I, J) = (1001, 481)$ is confirmed to be sufficiently accurate by comparing with those with grid points refined in either x or y direction.

- [1] Y. Zhou, *Phys. Rep.* **720-722**, 1 (2017).
- [2] Y. Zhou, *Phys. Rep.* **723-725**, 1 (2017).
- [3] Y. Zhou, T. T. Clark, D. S. Clark, S. G. Glendinning, M. A. Skinner, C. M. Huntington, O. A. Hurricane, A. M. Dimits, and B. A. Remington, *Phys. Plasmas* **26**, 080901 (2019).
- [4] D. L. Youngs, *Physica D* **12**, 32 (1991).
- [5] G. Dimonte and M. Schneider, *Phys. Rev. E* **54**, 3740 (1996).
- [6] V. N. Goncharov, *Phys. Rev. Lett.* **88**, 134502 (2002).
- [7] H. G. Lee and J. Kim, *Comput. Math. Appl.* **66**, 1466 (2013).
- [8] W. Liu, X. Wang, X. Liu, C. Yu, M. Fang, and W. Ye, *Sci. Rep.* **10**, 4201 (2020).
- [9] A. Benerjee, *J. Fluids Eng.* **142**, 120801 (2020).
- [10] O. Schilling, *J. Fluids Eng.* **142**, 120802 (2020).
- [11] Y. Zhou, R. J. R. Williams, P. Ramaprabhu, M. Groom, B. Thornber, A. Hillier, W. Mostert, B. Rollin, S. Balachandar, P. D. Powell, A. Mahalov, and N. Attal, *Physica D* **423**, 132838 (2021).
- [12] Lord Rayleigh, *Proc. Lond. Math. Soc.* **14**, 170 (1883).
- [13] G. I. Taylor, *Proc. R. Soc. Lond. Ser. A* **201**, 192 (1950).
- [14] C. X. Yu, C. Xue, J. Liu, X. Y. Hu, Y. Y. Liu, W. H. Ye, L. F. Wang, J. F. Wu, and Z. F. Fan, *Phys. Rev. E* **97**, 013102 (2018).
- [15] M. Dong, Z. Fan, and C. Yu, *Phys. Rev. E* **99**, 013109 (2019).
- [16] Z. F. Fan and M. Dong, *Phys. Rev. E* **101**, 063103 (2020).
- [17] K. Nishihara and T. Ikegawa, *J. Plasma Fusion Res. Ser.* **2**, 536 (1999).
- [18] Q. Zhang, *Phys. Rev. Lett.* **81**, 3391 (1998).
- [19] G. Dimonte, D. L. Youngs, A. Dimits, S. Weber, M. Marinak, S. Wunsch, C. Garasi, A. Robinson, M. J. Andrews, P. Ramaprabhu, A. C. Calder, B. Fryxell, J. Biello, L. Dursi, P. MacNeice, K. Olson, P. Picker, R. Rosner, F. Timmes, H. Tufo *et al.*, *Phys. Fluids* **16**, 1668 (2004).
- [20] G. Dimonte, P. Ramaprabhu, D. L. Youngs, M. J. Andrews, and R. Rosner, *Phys. Plasmas* **12**, 056301 (2005).
- [21] A. W. Cook, W. Cabot, and P. Miller, *J. Fluid Mech.* **511**, 333 (2004).
- [22] K. I. Read, *Physica D* **12**, 45 (1984).
- [23] D. L. Youngs, *Physica D* **37**, 270 (1989).
- [24] D. M. Snider and M. J. Andrews, *Phys. Fluids* **6**, 3324 (1994).
- [25] T. Wei and D. Livescu, *Phys. Rev. E* **86**, 046405 (2012).
- [26] X. Bian, H. Aluie, D. Zhao, H. Zhang, and D. Livescu, *Physica D* **403**, 132250 (2020).
- [27] R. M. Davies and G. I. Taylor, *Proc. R. Soc. Ser. A* **200**, 375 (1950).
- [28] P. R. Garabedian, *Proc. R. Soc. Ser. A* **241**, 423 (1957).
- [29] S. I. Abarzhi, *Phys. Rev. Lett.* **81**, 337 (1998).
- [30] Z. Jia, *J. Comput. Appl. Math.* **236** (2012).
- [31] M. S. Roberts and J. W. Jacobs, *J. Fluid Mech.* **787**, 50 (2016).
- [32] L. Duchemin, C. Josserand, and P. Clavin, *Phys. Rev. Lett.* **94**, 224501 (2005).
- [33] S. Abarzhi and K. C. Williams, *Phys. Plasmas* **27**, 072107 (2020).